Supplemental content: Effects of multi-jet coupling on propulsive performance in underwater pulsed jets

Athanasios G. Athanassiadis and Douglas P. Hart
(Dated: June 14, 2016)

I. ADDITIONAL EXPERIMENT DETAILS

A. Nozzles Fabrication

The nozzle bores were machined out to the final diameter from stock with a smaller bore. The outer diameter of the nozzles was 9.52mm, and the faces of the nozzles were machined smooth and deburred, but were not tapered to a fine angle or sharp edge as in other experiments [1–3]. The reservoir was connected to the nozzle with 6.35mm Tygon tubing. Differences in the machining of the two nozzles caused variations in the wakes generated by each nozzle. These differences caused the measurements of wake velocity and thrust to vary slightly between the two nozzles. As described in the text, the effects are accounted for by normalizing the measurements by the single-jet quantity for each jet.

B. Nozzle Positioning and Driving Pressure

In our experiment, the separation between the tank walls and the nozzle was 120mm, and the nozzle exit plane was submerged 40mm below the free surface. With this configuration, edge-effects are considered negligible during the vortex formation.

During a typical experiment, the height of the fluid in the reservoirs changed by less than 0.5mm, allowing the change in pressure head from surface motion to be ignored relative to the total reservoir height. The reservoirs were elevated $H = 570$mm above the water surface for an expected pressure head of $p_h = \rho g H \approx 5500$Pa. However, as described in the Supplemental Materials, losses between the reservoir and the nozzle reduced the effective pressure head to $p_{h,eff} \approx 114$Pa.

Given the geometry, the hydrostatic pressure at the nozzle exit is $p_{n,g} = \rho g(40\text{mm}) = 392$Pa. Because of the pressure loss through the tubing and valve, the effective driving pressure was estimated using a simplified momentum equation for unsteady pipe flow:

$$p_d - p_{n,g} \approx \frac{\rho u_j H}{t} = 114\text{Pa}.$$

C. Jet Velocity

To support our claim in the text that the jet velocities were nearly linear over the course of our experiment, Fig. S1a shows a typical trace of the flow-meter output for two single-nozzle experiments. As the nozzle spacing was varied, we observed no meaningful change in the jet velocity for either nozzle.

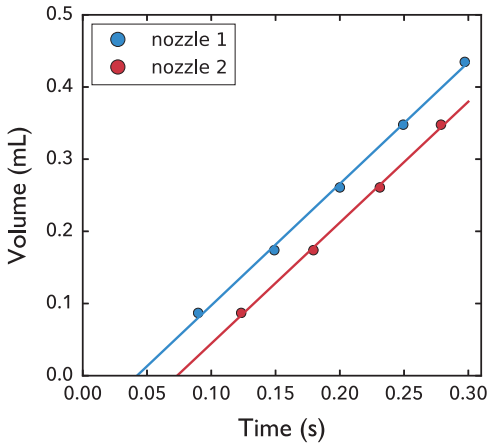

FIG. S1. Volume flux through the nozzle as measured by the flow meters attached to each reservoir. The volume flow through the nozzles is approximately linear in time, so to calculate the volume flow rate, the data for each nozzle are fit to a line. Here, the volume flow rate through each nozzle is $\dot{Q} = 1.68 \pm 0.04$mL/s. The vertical offset of the two traces reflects different initial readings in the flow meters, which are irrelevant for the flow rate calculations.

D. Optical Filtering

To prevent scattered laser light from affecting the optical signal, a 495nm optical high-pass filter (Thorlabs FGL495S) was placed in front of the camera.

II. ANALYSIS OF UNSTEADY THRUST TERM

Our dye-based analysis requires a way to calculate the unsteady term in the $\hat{\mathbf{z}}$ momentum equation, which is reproduced here for convenience:

$$\frac{d}{dt}\int_{\Omega_{cv}} \rho \mathbf{u}\cdot\hat{\mathbf{z}}\; dV.$$

As written, this term requires knowledge of the velocity field $\mathbf{u}$ everywhere within the control volume, which is not accessible through our dye measurements.

In order to measure flow unsteadiness from dye motion, we rewrite the integral in a Lagrangian formulation so that the local velocity u_z is the time derivative of the $\hat{\mathbf{z}}$ position of a particle within the CV. Then, we can write:

$$\begin{aligned}\int_{\Omega_{cv}(t)} u_z\, dV &= \int_{\Omega_{cv}(t)} \frac{\partial Z(\mathbf{r},t)}{\partial t}\, dV \\ &= \frac{d}{dt}\left[\int_{\Omega_{cv}(t)} Z\; dV\right] - \oint_{S_{cv}(t)} Z\;(\mathbf{u}\cdot\hat{\mathbf{n}})\; dA \\ &= \frac{d}{dt}\left[z_{cm}V_{cv}\right]\end{aligned}$$

The jump from the first to second line is made using the Reynolds Transport Theorem. We expect the surface integral to be zero because the control surface tracks the dye motion

(this assumption validated below). The final step is completed by observing that the integral in the first term is related to the $\hat{\mathbf{z}}$ position of the center of mass

$$z_{cm} = \frac{1}{V_{cv}} \int_{\Omega_{cv}} Z dV.$$

Inserting this derived quantity into the unsteady term above yields the result claimed in the main text:

$$\frac{d}{dt} \int_{\Omega_{cv}} \rho \mathbf{u} \cdot \hat{\mathbf{z}} \, dV = \frac{d^2}{dt^2} [z_{cm} V_{cv}] = \dot{u}_{cm} V_{cv} + 2 u_{cm} \dot{V}_{cv} + z_{cm} \ddot{V}_{cv}. \tag{S2.1}$$

We validated this analysis using 2D finite-volume simulations of a jet exiting a nozzle. By inserting a passive tracer into the nozzle before initiating flow, we can calculate a control volume equivalent to the one used in the experiments. This control volume was then used to calculate the unsteady term by directly integrating the flow field, as well as by using the CV volume and center of mass position. The two independent approaches produced identical results as shown in Fig. S2.

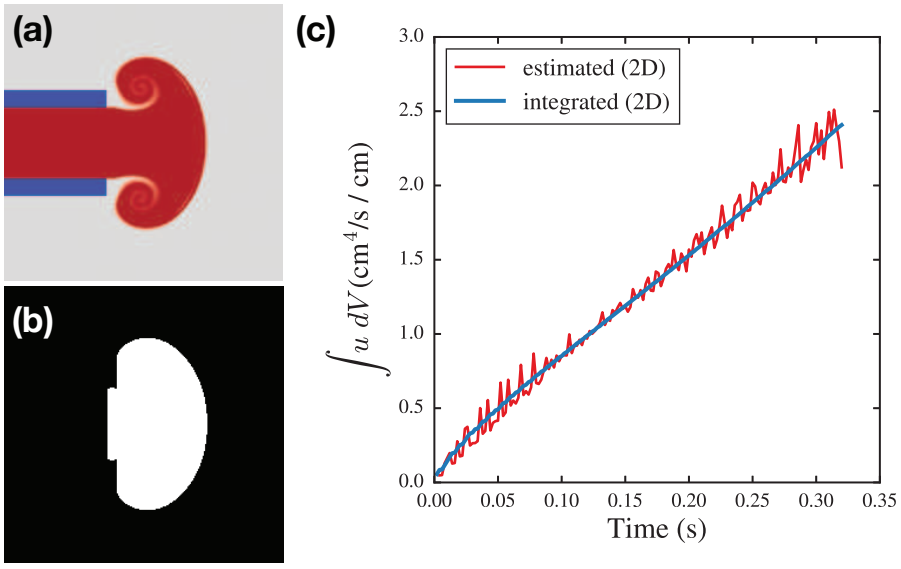

FIG. S2. Results of a 2D simulation used to verify our simplification of the unsteady integral. **(a)** A passive tracer is convected in the simulated flow to produce an image that can be tracked like the experiments. **(b)** Using the same analysis technique as for the experiments, the control volume is defined based on the dye location. **(c)** Comparison between direct integration of the velocity field within the CV and our estimate for the integral (S2.1). The two calculation techniques overlap exactly within numerical fluctuations that arise from the discrete derivatives required by our simplification.

III. VIDEO PROCESSING

A. Segmentation and Region Identification

Once the images are aligned and preprocessed, they are filtered and segmented using a local Otsu threshold [4, 5] to identify the regions of dyed fluid. The segmented regions are finally filtered with a horizontal hole-filling algorithm to produce a control volume such as the one shown in Fig. 3c in the main text.

The ellipsoid is identified such that the ellipsoid major radius b is half of the maximum wake width. The minor axis a lies along the nozzle centerline from the major axis to the leading edge of the wake. Since the wake is assumed to be axisymmetric, these two axes uniquely define the bounding ellipsoid as shown on the right of Fig. 3c in the main text.

IV. LEADING EDGE PRESSURE ESTIMATION TECHNIQUE

This approach was inspired by the work of Munk on potential flow around ellipsoids for airship design [6]. In order to compute the last term of the thrust equation (Eq. 3 in the main text), we estimate the pressure on the leading edge of the control surface by evaluate the velocity potential ϕ around a translating oblate ellipsoid of revolution. Using the Bernoulli equation:

$$p_{vb} - p_0 = \frac{\rho}{2}(\nabla\phi)^2\Big|_{S_{vb}} + \rho\frac{\partial\phi}{\partial t}\Big|_{S_{vb}}. \tag{S4.1}$$

We now derive a technique to analytically evaluate the velocity potential in terms of ellipsoid geometry (principal axes a along $\hat{\mathbf{z}}$ and b along $\hat{\mathbf{r}}$) and velocity ($w\hat{\mathbf{z}}$), which are measured as a function of time based on dye motion.

As given by Lamb, the velocity potential for a translating ellipsoid with principal radii a in the $\hat{\mathbf{z}}$ direction, b in the $\hat{\mathbf{y}}$ direction, and c in the $\hat{\mathbf{x}}$ direction, moving at velocity w in the $+\hat{\mathbf{z}}$-direction is most efficiently described in ellipsoidal coordinates [7]:

$$\phi(x,y,z,t) = -z \;\cdot\; \underbrace{\frac{w}{2-\alpha_0}}_{C(t)} \;\cdot\; \underbrace{abc\int_\lambda^\infty \frac{d\lambda'}{(a^2+\lambda')^{3/2}(b^2+\lambda')^{1/2}(c^2+\lambda')^{1/2}}}_{\alpha(\lambda,a,b,c;t)}. \tag{S4.2}$$

In Eq. S4.2, λ is the ellipsoidal coordinate that grows perpendicular to the ellipsoid with principal radii (c,b,a) along (x,y,z) respectively. As shorthand for the different terms in Eq. S4.2 I introduce the definitions:

$$C(t) = \frac{w}{2-\alpha_0}, \tag{S4.3}$$

$$\alpha_0 = \alpha(0,a,b,c;\ t), \text{ and} \tag{S4.4}$$

$$\alpha(\lambda,a,b,c;\ t) = abc\int_\lambda^\infty \frac{d\lambda'}{(a^2+\lambda')^{3/2}(b^2+\lambda')^{1/2}(c^2+\lambda')^{1/2}} \tag{S4.5}$$

It should be noted that x, y, z and λ are defined with respect to the moving ellipsoid center. It therefore makes sense to consider the equivalent problem of the ellipsoid in an unsteady free-stream flow with changing velocity $-w(t)\ \hat{\mathbf{z}}$.

A point in ellipsoidal coordinates is defined by the variables (λ, μ, ν) such that surfaces of constant λ are ellipsoids offset from the primary ellipsoid with principal radii (c, b, a) in the (x, y, z) directions respectively. To convert a point (x, y, z) from cartesian coordinates into ellipsoidal coordinates, the variables λ, μ, ν can be found as the solutions of the third-order polynomial in k defined by:

$$\frac{z^2}{a^2+k} + \frac{y^2}{b^2+k} + \frac{x^2}{c^2+k} - 1 = 0.$$

Canonically, the solutions for k are sorted so that $\lambda > \mu > \nu$. With this sorting, λ represents the spatial variable that increases perpendicular to the ellipsoid surface; surfaces of constant λ take the form of ellipsoids with scaled principle radii. The surface $\lambda = 0$ lays coincident with the surface of the ellipsoid (c, b, a).

For the case of an oblate ellipsoid of revolution (about the $\hat{\mathbf{z}}$ axis) with $a < b$, $b = c$ and $x^2 + y^2 = r^2$, this equation reduces to:

$$\frac{z^2}{a^2+k} + \frac{r^2}{b^2+k} - 1 = 0. \tag{S4.6}$$

Since we are only interested in the pressure on the surface ($\lambda = 0$) of such an oblate, axisymmetric ellipsoid translating along $\hat{\mathbf{z}}$, we can also use these assumptions to simplify Eq. S4.2:

$$\phi(x, y, z, t) = -z \cdot C(w, a, b; t) \cdot \alpha(\lambda = 0, a, b;\ z, r, t). \tag{S4.7}$$

Furthermore, this simplification admits the following closed-form solution to the integral:

$$\begin{aligned}
&\alpha(\lambda, a, b;\ t) \\
&\quad = ab^2 \int_\lambda^\infty \frac{d\lambda'}{(a^2+\lambda')^{3/2}(b^2+\lambda)} && \text{(S4.8)} \\
&\quad = ab^2 \left[-\frac{\pi}{(b^2-a^2)^{3/2}} + \frac{2}{(b^2-a^2)(a^2+\lambda)^{1/2}} + \frac{2\tan^{-1}\left(\sqrt{\frac{a^2+\lambda}{b^2-a^2}}\right)}{(b^2-a^2)^{3/2}} \right]. && \text{(S4.9)}
\end{aligned}$$

The integral α relates to the Bessel added mass k_z, for the ellipsoid moving in the z-direction, according to [7]:

$$k_z = \frac{\alpha_0}{2 - \alpha_0} \tag{S4.10}$$

Using this relationship, it can be shown that the closed form solution Eq. S4.9 approaches the expected limits as $a \to 0$ and $a \to b$, corresponding to a flat plate and a sphere respectively.

From these simplifications, it is possible to explicitly calculate the pressure on the surface of the vortex bubble using only the measured motion and growth of the ellipsoid bounding the vortex bubble. To calculate the spatial derivative required by the equation (Eq. S4.1) I observe that the only spatially dependent terms in Eq. S4.7 are C and α so that:

$$\nabla\phi(t)\Big|_{S_{vb}} = -\hat{\mathbf{z}} \cdot C(w, a, b; t) \cdot \alpha_0(a, b, t) - z \cdot C(w, a, b; t) \cdot \frac{\partial\alpha}{\partial\lambda}\Big|_{\lambda=0} \cdot \left(\hat{\mathbf{z}} \frac{\partial\lambda}{\partial z}\Big|_{\lambda=0} + \hat{\mathbf{r}} \frac{\partial\lambda}{\partial r}\Big|_{\lambda=0} \right).$$

The derivative $\partial\alpha/\partial\lambda$ can be evaluated by applying the fundamental theorem of calculus to Eq. S4.8. The spatial derivatives of λ can then be calculated by implicitly differentiating Eq. S4.6 with $k \equiv \lambda$. To calculate the time derivative of the velocity potential on the surface of the ellipsoid, the chain rule can be applied to ϕ :

$$\frac{\partial\phi}{\partial t}\Big|_{S_{vb}} = -z \cdot \alpha(0,a,b;t) \cdot \left(\frac{\partial C}{\partial w}\dot{u}_{vb} + \frac{\partial C}{\partial a}\dot{a} + \frac{\partial C}{\partial b}\dot{b}\right) - z \cdot C(w,a,b;t) \cdot \left(\frac{\partial \alpha}{\partial a}\dot{a} + \frac{\partial \alpha}{\partial b}\dot{b}\right)\Big|_{\lambda=0}.$$

Here, derivatives with respect to w, a, and b can be evaluated using Eqs. S4.3,S4.4, and S4.9.

Once these two derivatives are calculated, they can be inserted into the Bernoulli equation to estimate the pressure on the leading surface of the vortex bubble.

V. DERIVATION OF INDUCED VELOCITY SCALING

To describe the coupling of two simultaneous jets, we propose that the over-pressure at each nozzle is modified by the "induced" pressure, $p_{ind} \sim \rho u_{ind}^2$, associated with the other jet's developing vortex ring. Here, we derive our scaling for the induced velocity, $u_{ind} \sim r^{-3}$.

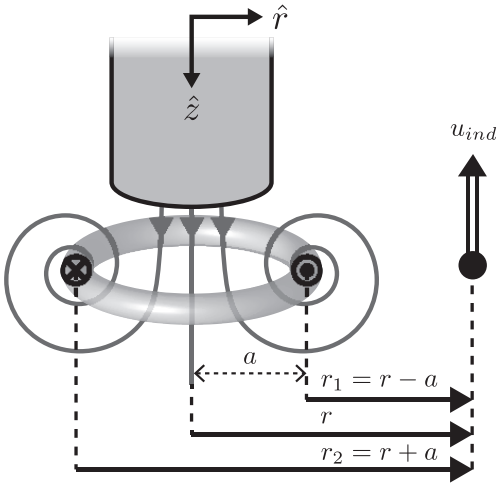

FIG. S3. Geometry for induced velocity derivation.

In 3D, a toroidal vortex ring with circulation Γ and radius a is described exactly by the axisymmetric stream function (See Lamb [7], Art. 161):

$$\psi(r,z) = -\frac{\Gamma}{2\pi}(r_1 + r_2)\left[K(\lambda) - E(\lambda)\right] \tag{S5.1}$$

where

$$\lambda = \frac{r_2 - r_1}{r_2 + r_1}, \qquad r_1^2 = z^2 + (r-a)^2, \quad \text{and} \quad r_2^2 = z^2 + (r+a)^2$$

As shown in Fig. S3, r_1 is the closest distance of the vortex ring to the field point (r, z), and r_2 is the farthest distance. K and E are complete elliptic integrals of the first and second kind, respectively.

Since the two vortex rings form simultaneously, we expect that their mutual effects are dominant on the plane $z = 0$. In this case, the induced velocity is antiparallel to $\hat{\mathbf{z}}$, $r_1 = r - a$, $r_2 = r + a$, and $\lambda = a/r = D/(2r)$. Differentiating the stream function yields a result for the velocity induced by a developing vortex ring:

$$\mathbf{u}_{ind}(r, z = 0) = \frac{1}{r}\frac{\partial \psi}{\partial r}\hat{\mathbf{z}} = -\hat{\mathbf{z}}\left(\frac{2\Gamma}{\pi D}\right)\lambda\left[K(\lambda) - \frac{2-\lambda}{2(1-\lambda)}E(\lambda)\right]. \tag{S5.2}$$

The complete elliptic integrals can be expanded in a power series about $\lambda = 0$ [8]:

$$K(\lambda) = \frac{\pi}{2}\left[1 + \frac{1}{4}\lambda^2 + O(\lambda^4)\right] \qquad E(\lambda) = \frac{\pi}{2}\left[1 - \frac{1}{4}\lambda^2 - O(\lambda^4)\right].$$

Inserting these expressions into Eq. S5.2, expanding u_{ind}, and substituting $\lambda = D/(2r)$, the induced velocity can be written to leading order as

$$\mathbf{u}_{ind}(r) \approx (-\hat{\mathbf{z}})\left(\frac{\Gamma}{2D}\right)\left(\frac{D}{r}\right)^3. \tag{S5.3}$$

This leading order scaling is valid as long as $\lambda \ll 1$. As $\lambda \to 1$, u_{ind} diverges to $+\infty$ and higher order terms dominate. In terms of r/D, the higher order terms should be negligible until $r/D \lesssim 1$. In the regime of our experimental data, $r/D \gtrsim 1.7$, the next term, of $O(r^{-4})$, is 3 times smaller than the leading order term. Hence we describe the physics of the two-jet coupling using the leading-order approximation, $u_{ind} \sim r^{-3}$.

VI. ADDITIONAL MEASUREMENTS

A. Wake Kinematics

In our analysis, we asserted that the z-position and volume of the control volume grow linearly with time, so that higher order derivatives such as $\dot{u}_{cm}$ and $\ddot{V}_{cv}$ could be ignored. Here we provide typical data to support this claim. As shown in Fig. S5, both position and volume are roughly linear across the time range measured. Small sinusoidal oscillations arise in the plots from a shear instability along the jet (visible in the videos). By fitting these quantities to a line, the oscillations are suppressed. While the wake position and volume are roughly linear over the experiment, the vortex bubble shape is not. The major and minor radius of the bounding ellipsoid are tracked during the experiments, and their values are used directly to compute the time-dependent pressure on the leading edge of the wake.

B. Thrust

In the main text, we showed only normalized thrust measurements, $T(\widetilde{\Delta})/T_\infty$, but claim that the contribution from the pressure integral is an order of magnitude smaller than the contribution from unsteadiness in the wake. In Fig. S4, we provide the data to support this claim.

[1] Paul S Krueger and M Gharib, "The significance of vortex ring formation to the impulse and thrust of a starting jet," Physics of Fluids **15**, 1271 (2003).
[2] Paul S Krueger and Morteza Gharib, "Thrust Augmentation and Vortex Ring Evolution in a Fully-Pulsed Jet," AIAA Journal **43**, 792–801 (2005).
[3] T Maxworthy, "The structure and stability of vortex rings," Journal of Fluid Mechanics (1972).
[4] N Otsu, "A threshold selection method from gray-level histograms," Automatica (1975).
[5] Stéfan van der Walt, Johannes L. Schönberger, Juan Nunez-Iglesias, François Boulogne, Joshua D. Warner, Neil Yager, Emmanuelle Gouillart, Tony Yu, and the scikit-image contributors, "scikit-image: image processing in Python," PeerJ **2**, e453 (2014).
[6] Max M Munk, *Remarks on the Pressure Distribution over the Surface of an Ellipsoid, Moving Translationally Through a Perfect Fluid*, Tech. Rep. 196 (National Advisory Committee for Aeronautics, 1924).
[7] Horace Lamb, *Hydrodynamics*, 6th ed., Vol. 8637 (Dover publications, New York,, 1945).
[8] M D Friedman and M D Byrd, *Handbook of elliptic integrals for engineers and scientists*, Vol. 67 (Springer-Verlag Berlin Heidelberg, Berlin, Heidelberg, 1971).

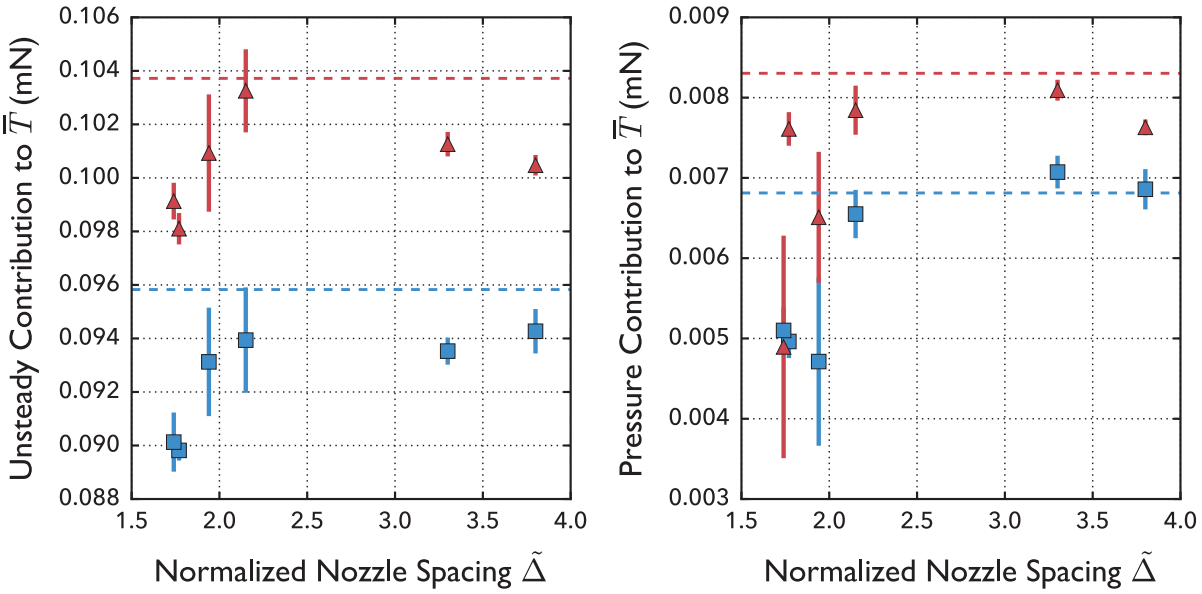

FIG. S4. Contribution of the two different terms, unsteady and surface pressure, to the thrust measurement. Points represent the average of 5 experiments for each value of $\tilde{\Delta}$. The dotted lines represent the average of 5 experiments for the single nozzle experiments - nozzle 2 is indicated by red and nozzle 1 is indicated by blue. The unsteady contribution is typically 10 times stronger than the pressure contribution.

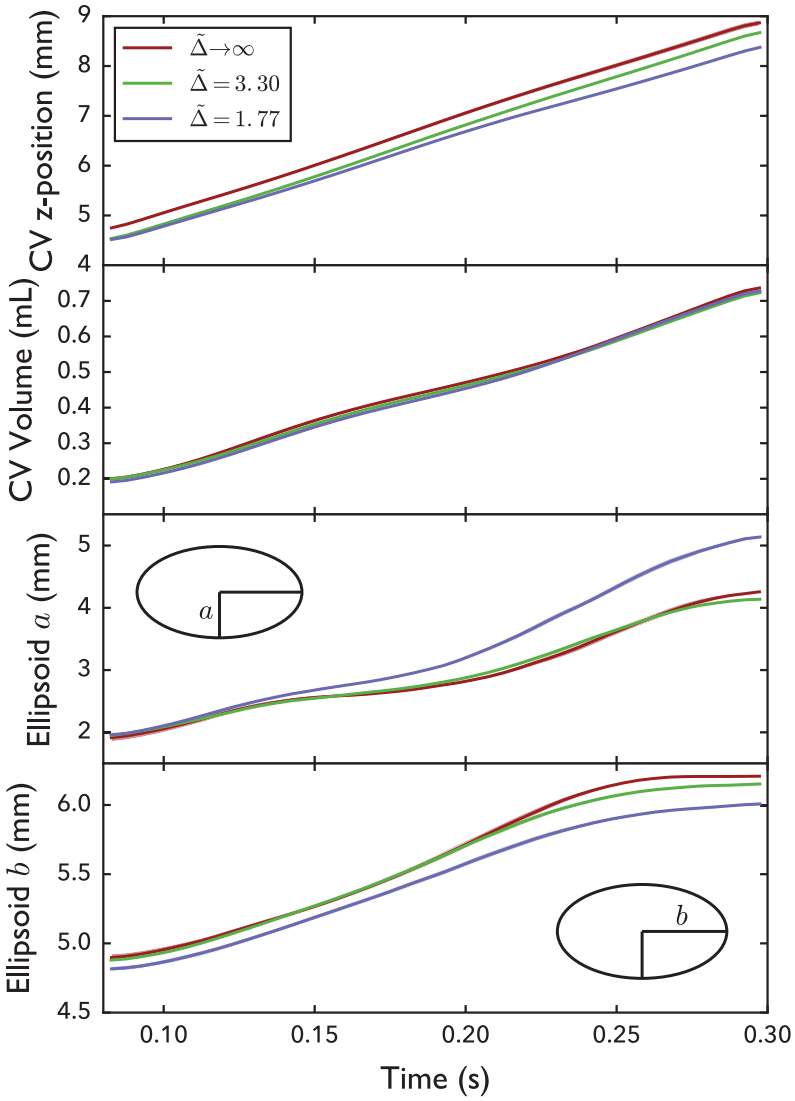

FIG. S5. Results of CV tracking for select experiments. Solid lines represent the median curve from 5 experiments, and the shaded regions represent one standard deviation. As indicated by the small error bars, these experiments produced highly repeatable results.